



Article

Wind Direction Extraction from X-Band Marine Radar Images Based on the Attenuation Horizontal Component

Huanyu Yu ¹, Zhizhong Lu ^{1,*} and Hui Wang ²

¹ College of Intelligent Systems Science and Engineering, Harbin Engineering University, No. 145 Nantong Street, Nangang District, Harbin 150001, China; yuhuanyu@hrbeu.edu.cn

² School of Naval Architecture and Ocean Engineering, Guangzhou Maritime University, No. 101 Hongshan 3rd Road, Huangpu District, Guangzhou 510725, China; wanghuijkd@just.edu.cn

* Correspondence: luzhizhong@hrbeu.edu.cn

Abstract: This paper presents a novel algorithm based on the attenuation horizontal component for wind direction retrieval from X-band marine radar images. The range dependence of radar return on the ocean surface can be presented in radar images, and the radar return decreases with the increase in range. The traditional curve-fitting method averages the radar return of the whole range to retrieve the wind direction, but it is vulnerable to the interference of fixed objects and long-range low-intensity pixel points. For the pixels with the same range in the polar coordinates of the radar image, the ideal range attenuation model is derived by selecting the pixels with the highest intensity value. The ideal attenuation model is used to fit the attenuation data and calculate the attenuation horizontal component at each azimuth direction. To eliminate the effect of outliers, the iterative optimization method is used in the estimation of the attenuation horizontal component and the weights of the data are continuously updated. Finally, the wind direction is determined based on the azimuthal dependence of the attenuation horizontal component. This algorithm was tested using shipboard radar images and anemometer data collected in the East China Sea. The results show that, compared with the single curve-fitting method, the proposed algorithm can improve the wind direction retrieval accuracy in the case of more fixed targets. Under the condition of more fixed targets, the deviation and root mean square error are reduced by 16.3° and 16.2°, respectively.



Citation: Yu, H.; Lu, Z.; Wang, H. Wind Direction Extraction from X-Band Marine Radar Images Based on the Attenuation Horizontal Component. *Remote Sens.* **2023**, *15*, 3959. <https://doi.org/10.3390/rs15163959>

Academic Editors: Reza Shahidi and Eric Gill

Received: 3 June 2023

Revised: 13 July 2023

Accepted: 8 August 2023

Published: 10 August 2023



Copyright: © 2023 by the authors. Licensee MDPI, Basel, Switzerland. This article is an open access article distributed under the terms and conditions of the Creative Commons Attribution (CC BY) license (<https://creativecommons.org/licenses/by/4.0/>).

Keywords: X-band marine radar; wind direction; radar return range attenuation; ideal attenuation model; attenuation horizontal component

1. Introduction

The sea surface wind field is an important parameter in the study of the interaction between the air and the sea, and regulates the coupling between the atmosphere and the ocean by adjusting heat, water vapor, and particulate matter, thereby maintaining the global and regional climate. Wind direction is now mainly measured using in situ sensors located on the ship's mast, such as the anemometer; however, the anemometer is susceptible to atmospheric turbulence and turbulent airflow caused by the ship's superstructure. Even if the anemometer is installed in an unobstructed position, the error in the measurement of the wind direction can be very high [1,2]. In recent decades, marine radar has become an effective method for obtaining sea surface wind field information due to its advantages of high resolution and timely feedback [3]. Moreover, most ships have been equipped with marine radar, which has a small additional cost compared with other remote sensing instruments. To date, X-band marine radar has been widely used to detect the current [4–9], bathymetric data [10–16], and waves [17–24], and significant progress has been achieved in this field. However, the extraction of wind parameters using X-band marine radars still needs further refinement.

Marine radar generally works under the grazing incidence and emits X-band electromagnetic waves to the sea surface in a rotating manner. The radar backscattering from

the sea surface is mainly produced by the Bragg resonance interaction between the electromagnetic wave and the high-frequency gravity–capillary wave affected by gravity and surface tension [25,26], which is the basic theory of the marine radar telemetry sea surface. It has been shown [27,28] that X-band marine radar operating under horizontal polarization (HH) has only one peak of radar return intensity from the ocean surface, i.e., the upwind direction. Therefore, the wind direction can be retrieved using the relationship between the radar return and the azimuth of the radar antenna. Based on this principle, there are two main types of wind direction extraction. One type uses integrated radar image sequences to obtain the wind direction [29,30], while the other type requires only a single radar image to directly retrieve the wind direction [31–33]. The above methods can retrieve wind direction well in the absence of rain, but rainfall causes severe interference in radar imaging [34–36]. Therefore, in recent years, retrieval of the wind direction from rain-contaminated radar images has become the main research direction, and great progress has been made [37–40]. Another algorithm is based on wind streaks that are visible in time-integrated X-band marine radar images and aligned with the average wind direction [26]. Based on the wind streak theory, the optical flow motion estimation-based technique (OFM) [41] and the local gradient method (LGM) [42–44] were proposed. However, the results of the OFM algorithm are not accurate and difficult to achieve in engineering. LGM requires sub-sampling of the wind stripe image. Accurate wind direction results can only be obtained when the image resolution is reduced to 1/16–1/4 of the wind streak scale. In addition, the scale of the wind streak is 200–500 m, and it is uncertain, so it is difficult to retrieve the accurate wind direction.

In the above developments, not only has the obstructed radar field of view been considered, but also the azimuth of the obstructed wind direction. In addition, during radar image preprocessing, the interference of fixed objects is removed by setting a threshold. Although satisfactory results are obtained in a large range of wind directions and wind speeds, different thresholds need to be set for different radars and are not robust. Ships sailing on the sea surface will encounter a variety of sea conditions which appear on the marine radar image, and images are especially vulnerable to the sudden appearance of fixed objects and other outliers on the sea surface. However, there is not only the effect of occlusion by fixed targets, but also the occlusion of shadows formed behind the targets. It is difficult to calculate the true average radar return intensity even if the pixel points of the targets are excluded, i.e., there are local low or high values. Hence, although the data of the occlusion direction are excluded, the data generated by complex sea conditions may be retained, resulting in less accurate results. Furthermore, the radar return intensity is modulated by range, and the radar return attenuates with increasing range distance in radar images [28]. At longer range, the surface signal not only decreases with increasing range, but there are more pixels with low-intensity values. This is one of the reasons for the reduced retrieval accuracy of the wind direction. It has been proven that any range dependence occurring in radar images is the result of the grazing angle dependence on the radar return on the ocean surface, which has a cubic relationship with range [28]. Subsequently, the radar return was derived as the modeled function of range using the best fit in the retrieval of sea surface wind parameters [31]. In summary, the interference of outliers and fixed targets in the radar image cannot be ignored, nor the excessive low-intensity points caused by radar return range attenuation when the wind direction is retrieved from marine radar images. In addition, it is necessary to find a technology that can process complex sea surface abnormal values in a stable manner and extract wind direction.

To overcome the uncertain interference in radar images, this paper proposes an algorithm based on the attenuation horizontal component for wind direction retrieval from X-band marine radar images. This is the first time that the range attenuation property of the radar return has been used to extract the sea surface wind direction. The algorithm first needs to determine the ideal attenuation model of the radar image, and then uses the ideal range attenuation model for comparison with one-dimensional data to find the

relative difference value at each azimuth direction, i.e., the attenuation horizontal component. In addition, the algorithm removes outliers and low-intensity invalid points by updating weights and thresholds during iterative optimization, without judgement during preprocessing. To improve the stability of the wind direction retrieval, the cosine square function proposed in [31] is improved when applied to the wind direction estimation. Finally, the wind direction is retrieved by using the attenuation horizontal component as an improved cosine function of the azimuth direction. Since the ideal attenuation model has the same attenuation trend as the one-dimensional data of each azimuth, sudden outliers (such as fixed targets and local occlusion areas) can be stably excluded by fitting; this is particularly the case for radar images with more fixed targets and local occlusion areas. In addition, their relative difference value (attenuation horizontal component) also retains the directional characteristic of the wind field, so that the sea surface wind direction can be stably retrieved. This study is organized as follows: Section 2 describes the wind direction retrieval algorithm, including data preprocessing, derivation of the ideal range attenuation model, extraction of the attenuation horizontal component, and wind direction retrieval. Experimental results, including the overview of the data, are presented in Section 3. The results are discussed in Section 4. Finally, a summary and future work are presented in Section 5.

2. Wind Direction Retrieval Methods

This section utilizes the range attenuation characteristic of radar return in X-band marine radar images to extract wind direction. Traditional methods of calculating wind direction may be hindered by fixed targets, high-frequency noise, and invalid low-intensity pixels. To overcome these limitations, the fixed targets are preliminarily removed based on histogram statistics, and subsequently an ideal range attenuation model of the radar image is established. This paper utilizes a comparison of one-dimensional attenuation data for each azimuth with the ideal attenuation model to determine the attenuation horizontal component relative to the ideal attenuation model. This is a constant of the one-dimensional attenuation data relative to the ideal range attenuation model at a certain azimuth. When the radar return in a certain azimuth is high, the corresponding horizontal component of attenuation is also high, and vice versa. By adding a threshold to the process of estimating the attenuation horizontal component for iterative optimization, the effects of the surrounding environment and low wind speed are further excluded. The extracted attenuation horizontal component retains its dependence on the azimuth; thus, the wind direction can be determined by retrieving the maximum attenuation horizontal component, taking into account the correlation between the attenuation horizontal component and the azimuth angle. The flow chart of the wind direction extraction process is given in Figure 1.

2.1. Data Preprocessing

Radial noise lines caused by interference from other marine radars appear as high-intensity pixel lines distributed along the range direction in radar images [38]. Given that the marine radar data used in this study come from the same equipment as that used in [33], median filtering is applied here to remove the interference caused by radial noise lines. A 3×3 sliding template is selected, and each pixel is replaced with the median radar return value of the remaining eight image points within the adjacent window for that point. To make better use of the data, the radar image data is normalized by converting the radar return data to decimal values between 0 and 1. In this study, the maximum–minimum normalization method is applied and is calculated as follows:

$$x_{\text{normalization}} = \frac{x - \min(x)}{\max(x) - \min(x)} \quad (1)$$

where x is the original image after median filtering and $x_{\text{normalization}}$ is the normalized radar image.

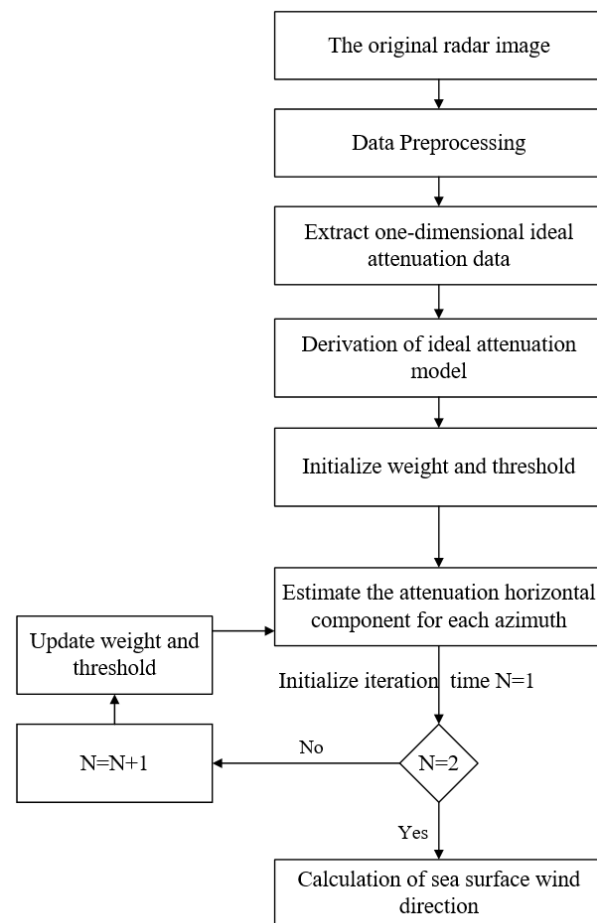


Figure 1. The flow chart of the wind direction extraction process.

2.2. Radar Return Ideal Range Attenuation Model

Similar to the range attenuation observed in radar images, the vignetting phenomenon is also present in conventional images, where the intensity of pixels attenuates radially from the center of the image to the periphery [45]. Therefore, a similar concept is introduced to model the range attenuation of radar images, as proposed in [46]:

$$X(r, \theta) = Y(r, \theta) \cdot D(r, \theta) \quad (2)$$

where X and Y represent the radar attenuation image and the potential range-free attenuation image in polar coordinates, respectively (the origin of which is the center of the radar image); D represents a one-dimensional attenuation function; θ is the angle between the scanning direction of the radar antenna and ship heading; and r is the range distance from the radar antenna to the sea surface.

It has been shown that range dependence observed in radar images is a direct result of the grazing angle dependence of radar return on the ocean surface, with the radar return being cubic-dependent on range [28]. Therefore, it can be considered that the range attenuation effect is the same at each azimuth of the radar image. In this study, one-dimensional data from one of the azimuths are chosen to represent the overall distribution of attenuation effects and to estimate the ideal range attenuation model. Figure 2 shows three different types of radar images. Figure 2a is a long-pulse radar image at low wind speed, Figure 2b is a short-pulse radar image with fixed targets at medium wind speed, and Figure 2c is a short-pulse radar image at high wind speed, but there are more fixed targets in the radar image. X-band marine radar images not only exhibit range attenuation characteristics but are also affected by wave shadow modulation, as illustrated in Figure 3a.

Consequently, the curve plotted at a fixed azimuth shows that the radar return intensity decays with range overall, while still moving up and down locally, as depicted in Figure 3b.

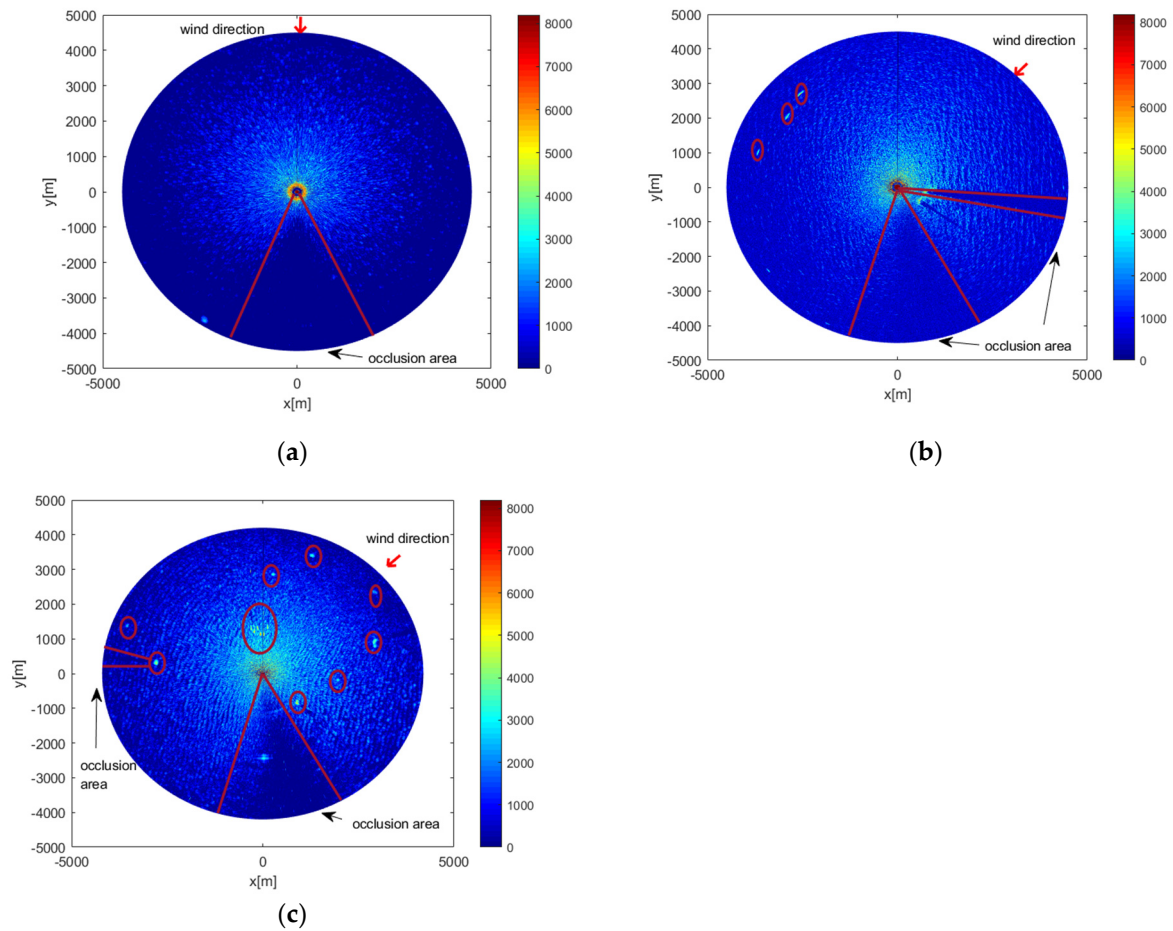


Figure 2. Three different kinds of radar images: (a) long-pulse image collected under low-wind-speed conditions (obtained on 21 September 2017 at 09:06), with a heading of 87.9° , a wind direction of 88.99° , and a wind speed of 5.9 m/s, as measured by an anemometer; the red line indicates the occlusion area; (b) short-pulse image collected under high-wind-speed conditions (obtained on 24 October 2017 at 03:27), with a heading of 347.3° , a wind direction of 31° , and a wind speed of 9.8 m/s, as measured by an anemometer; the oval indicates the ship; (c) short-pulse image collected under high-wind-speed conditions (obtained on 24 October 2017 at 06:42), with a heading of 1° , a wind direction of 50° , and a wind speed of 11 m/s, as measured by an anemometer; the oval indicates the ship.

To eliminate the effect of wave shadow modulation and only retain the characteristic of range attenuation, pixel points with the highest radar return value are selected from pixels with the same range in the radar image to derive the ideal attenuation data. The ideal attenuation data are determined as follows:

$$X_{ra}(r) = \max_{\theta} \{ (r, \theta) \} \theta \in [0, 360) \quad (3)$$

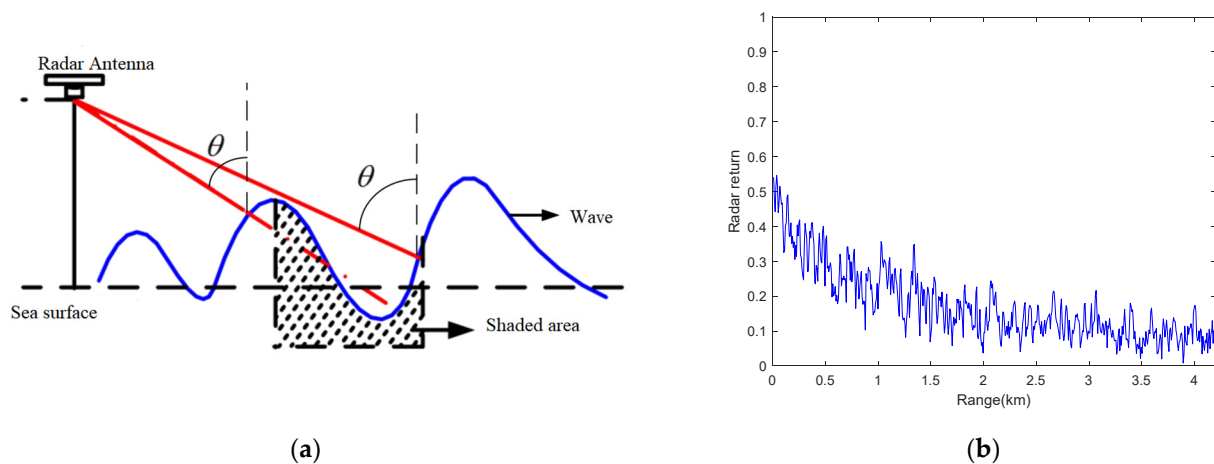


Figure 3. (a) Schemes of shadow modulation; (b) one-dimensional angle data randomly selected from Figure 2b.

To exclude fixed targets in the calculation process, histogram statistics are derived for all pixels in the same range r before extracting the ideal attenuation data. The radar return values belonging to range r are stored in a histogram of 256 bins ranging from 0 to 1. Then, each bin in the histogram is counted, and if the number belonging to a radar return value is less than the predetermined threshold T , this radar return value is considered as the target and excluded, as shown in Figure 4a. Finally, the maximum radar return intensity belonging to r is selected from the remaining radar return values. Because T is the threshold in the histogram statistics, it is set in relation to the number of pixel points in the radar image. A smaller threshold can eliminate outliers in the image to the greatest extent, and a larger threshold cannot eliminate the low proportion of outliers. Referring to [45] for the threshold settings, the radar image threshold is set to $T = 0.01 \times N$, where N is the number of radar image azimuths θ . Figure 4b shows the ideal attenuation data of Figure 2b after excluding outliers based on the histogram statistics, which only retains the attenuation characteristics of radar return. Figure 5 shows the radar image in Figure 2b,c in which the fixed targets are removed based on histogram statistics. It can be seen from the figure that fixed objects such as ships are excluded. The processed image is then used as the input for subsequent calculation.

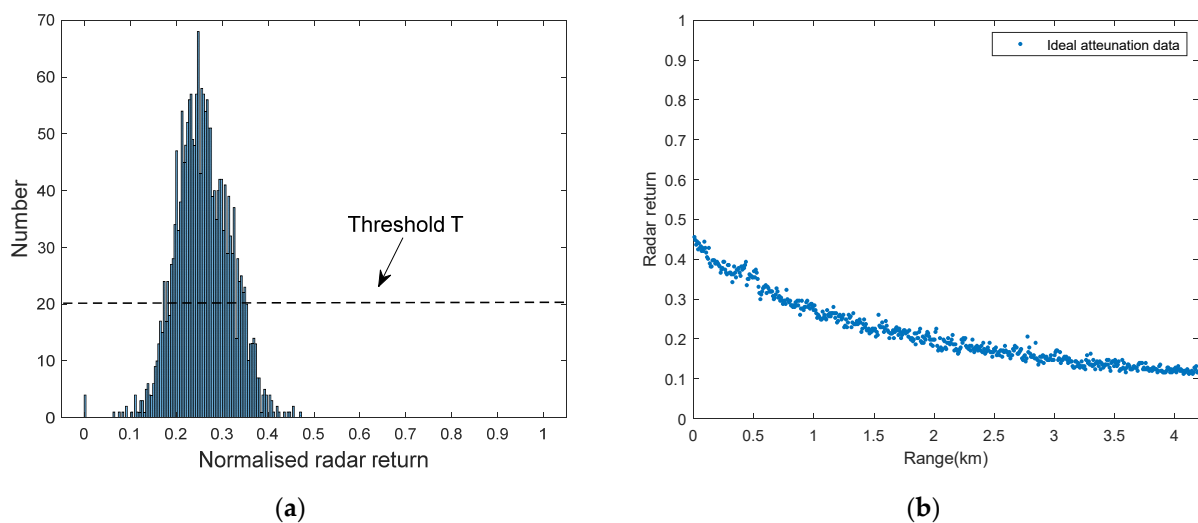


Figure 4. Extraction process of ideal attenuation data: (a) the histogram statistics of radar return at one range distance r for Figure 2b (the radar return values have been normalized); (b) the ideal attenuation data for Figure 2b.

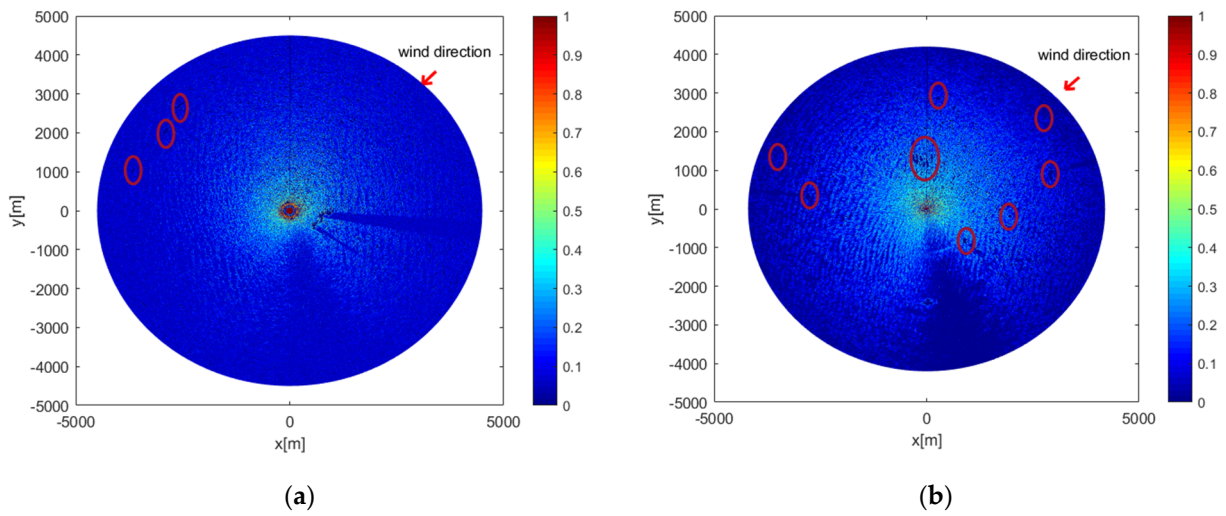


Figure 5. The radar image of (a) Figure 2b and (b) Figure 2c after excluding fixed targets based on histogram statistics.

After obtaining the ideal range attenuation data X_{ra} , the attenuation function model is fitted to the attenuation data using least-squares fitting to estimate the ideal range attenuation model D . This paper uses the improved model of Lund [31] to represent the ideal range attenuation model D , which is:

$$D(r) = \frac{b_0}{(1 + r^{b_1})} \tag{4}$$

where b_0 and b_1 are the regression parameters, and r is the range distance from the radar antenna. In this study, the attenuation model is limited to the range from 0 to b_0 . When the range distance is 0, there is no attenuation and the value of the attenuation function is b_0 , which is only related to the overall radar echo intensity. The overall echo intensity is mainly affected by the wind speed. Furthermore, the value of the attenuation function decreases with the increase in the distance range. By fitting the ideal attenuation data using Equation (4), an ideal attenuation model of a radar image can be obtained. Figure 6 shows the fitted ideal range attenuation model. Because the attenuation characteristics of each azimuth in a radar image are the same and have the same attenuation trend, the obtained ideal attenuation model is compared with the attenuation data of each azimuth in the radar image to obtain a relative difference value, that is, the attenuation horizontal component.

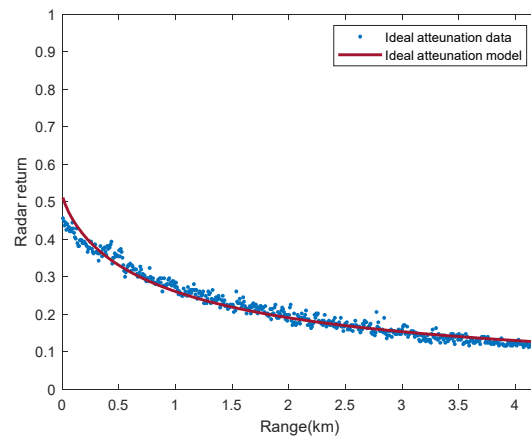


Figure 6. Ideal range attenuation model.

2.3. Estimation of Attenuation Horizontal Components and Outlier Treatment

The ideal attenuation model is implemented as a baseline to be compared and fit with the one-dimensional data at each azimuth, thereby deriving the attenuation horizontal components, which represent the difference between the one-dimensional attenuation data and the ideal attenuation model. Under ideal conditions, for one-dimensional data at a certain azimuth, the radar return intensity not only decreases with range but also correlates with wind speed and direction. The overall radar return intensity becomes stronger as the wind speed increases, but it maintains a stable range attenuation. A peak is observed in the radar return intensity when it is aligned with the wind direction. In addition, the non-attenuated radar image $Y(r, \theta)$ in Equation (2) has almost different horizontal lines in different azimuth directions θ , which are due to the influence of the wind direction. A relative difference value is derived by comparing one-dimensional data at a given azimuth to a fixed ideal range attenuation model, which is a constant and is defined in this paper as the attenuation horizontal component. Therefore, the attenuation horizontal component of each azimuth can be estimated by replacing $Y(r, \theta)$ with the constant C_θ and minimizing the following:

$$\operatorname{argmin}_{C_\theta} \sum_{r=0}^{r_{\max}} (|C_\theta D(r) - X(r, \theta)|) \quad (5)$$

However, the estimation process is disturbed by outliers in $X(r, \theta)$ such as noise, supersaturation, and low-intensity pixels caused by range attenuation. Unlike Equation (5), a continuously updated threshold δ and weight ω are used to exclude the interference of outliers, and C_θ can be estimated using Equation (6):

$$\operatorname{argmin}_{C_\theta} \left(\sum_{r=0}^{r_{\max}} \omega(r) \cdot \min(|C_\theta D(r) - X(r, \theta)|, \delta) \right), \text{ subject to } 0 \leq C_\theta \leq 1 \quad (6)$$

where ω is a weighted function and δ is the threshold. Because the range attenuation is more serious when r increases, a larger weight is given to the points away from the radar antenna when modeling the weighting function. Equation (7) is chosen to model the weights after testing:

$$\omega(r) = \frac{\sqrt{r/l}}{\sum_{n=1}^p \sqrt{n}} \quad (7)$$

where n is the discrete point position of range distance, l is the resolution of range distance, and p is the maximum discrete point position of range distance. Since the range of radar data is 0 to 1, the initial value of the threshold δ is set to 0.5 through experiments. In addition, the weights of the low-intensity points caused by range attenuation and other factors are set to zero. In this paper, pixel points with an intensity value less than 0.05 are considered invalid. The nonlinear least-squares method is used to solve Equation (6). However, due to outliers, the initial estimation results may be inaccurate. Therefore, the iterative optimization is used to update the value of C_θ . In the first iteration, δ is halved so that more unstable values will be determined and the weight is updated to exclude outliers such as high-intensity system noise and low-intensity points. The weight ω is updated by determining the outliers in $X(r, \theta)$ using Equation (8):

$$\omega(r) = \begin{cases} \omega(r), & \text{if } |C_\theta D(r) - X(r, \theta)| < \delta \\ 0, & \text{otherwise} \end{cases} \quad (8)$$

The updated parameters δ and ω are passed to the next iteration. The whole process is iterated two times to obtain the final attenuation horizontal components, as shown in Algorithm 1.

Algorithm 1: Estimation of attenuation horizontal components and outlier treatment

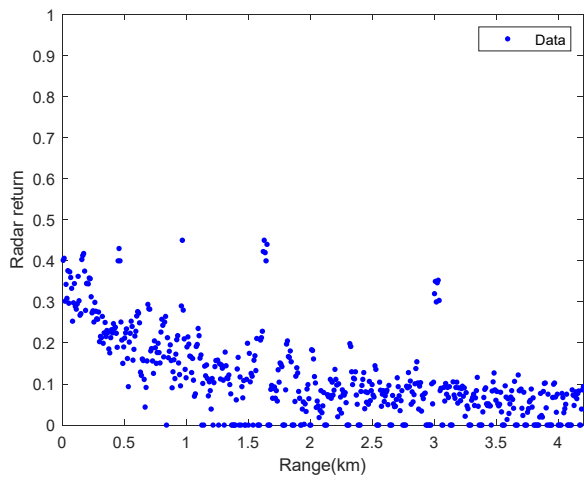
Input: ideal range attenuation model D
 $\delta = 0.5$, Initialize ω using Equation (7)
 $C_\theta \leftarrow$ Estimate the attenuation horizontal components preliminarily using Equation (6)
for $N = 1:2$
 $\delta \leftarrow \delta = \delta/2$
 $\omega \leftarrow$ Update ω with using Equation (8)
 $C_\theta \leftarrow$ Estimate the attenuation horizontal components using Equation (6)
end for
Output: C_θ

To clearly show the process of estimating the attenuation horizontal component and the treatment of outliers, one-dimensional data from two azimuths of Figure 2a,c are selected. The one-dimensional data selected in Figure 2a contain some high-intensity outliers, and the data selected in Figure 2c are one-dimensional data of about 290° which are not only affected by the high-intensity target, but also form a low-intensity occlusion area behind the target. Figure 7 shows the estimation process of an azimuth attenuation horizontal component, where Figure 7a–d show the estimation process of the one-dimensional data in Figure 2a, and Figure 7e–h show the estimation process of the one-dimensional data in Figure 2c. It can be observed from Figure 7a that there are many invalid low-intensity pixels and noises in the one-dimensional data, which will cause errors in the estimation of the attenuation horizontal component. In the process of initial estimation of the attenuation horizontal component, this part of the interference is eliminated by setting the weight of the low-intensity pixels to zero, as shown in Figure 7b. After two iterative optimizations in which the truncation distance δ is added, the interference in the one-dimensional attenuation data at the same azimuth angle is further eliminated, as shown in Figure 7c,d. It can be seen from Figure 2c that the high-intensity target will block the propagation direction of the electromagnetic wave and a local occlusion area appears behind it. In addition, it should be noted that the high-intensity target has been excluded based on the previous histogram statistics. As shown in Figure 7e, the occlusion area produces a large number of low-intensity pixel points, which will lead to errors in wind direction results. Combining Figure 7f–h, it can be seen that the low-intensity invalid points generated in the occlusion area are eliminated through initial estimation, and the attenuation horizontal component is updated through two iterations. Since there are only outliers formed by the occlusion area, the attenuation horizontal components calculated in the last two iterations are the same as the initial estimated values. At the same time, it can be observed that although there is a large deviation between the attenuation model and the data in the near ranges, it fits well in most ranges, so it has little effect on the extraction of the attenuation horizontal component. This mainly depends on the selection of the ideal attenuation model, and a better attenuation model needs to be found in subsequent research.

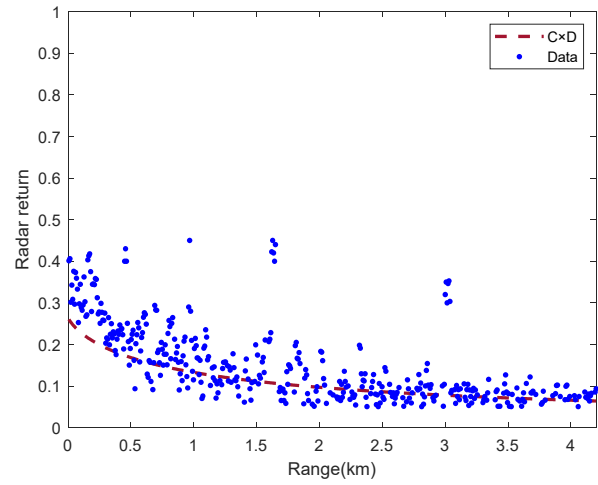
2.4. Wind Direction Extraction Method

Previous studies have shown that the maximum radar return from X-band marine radar operating under grazing incidence and HH polarization conditions occurs in the upwind direction. In order to improve the stability of wind direction estimation, the cosine square function of Lund is optimized. The improved formula is as follows:

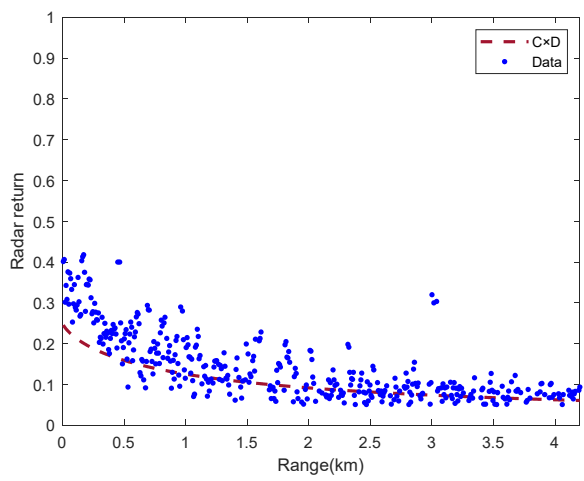
$$C_\theta = a_0 + a_1 \cos(\theta - a_2) \quad (9)$$



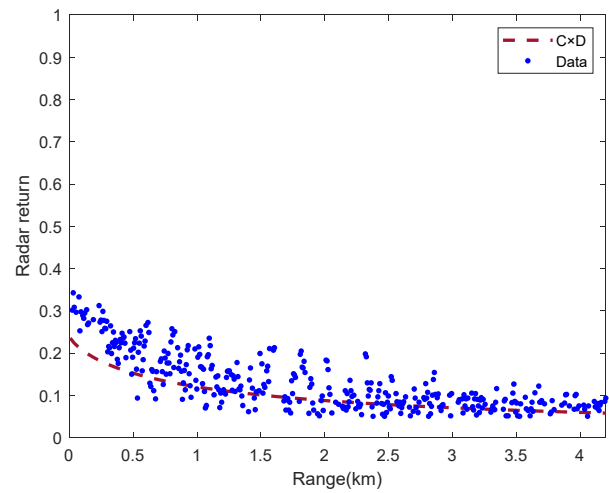
(a)



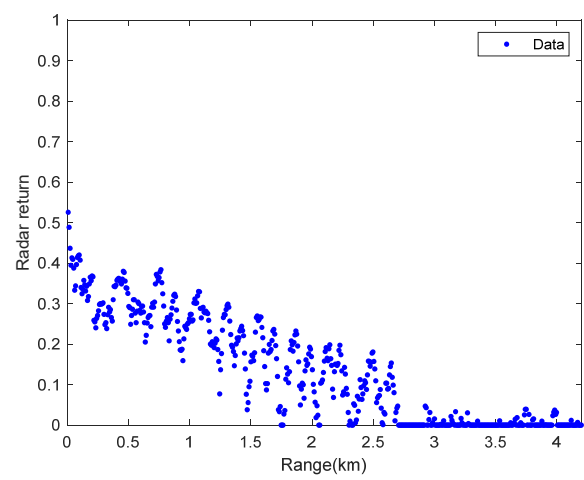
(b)



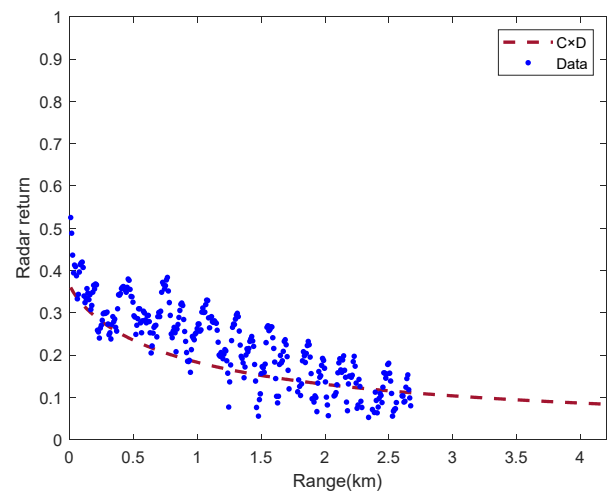
(c)



(d)



(e)



(f)

Figure 7. Cont.

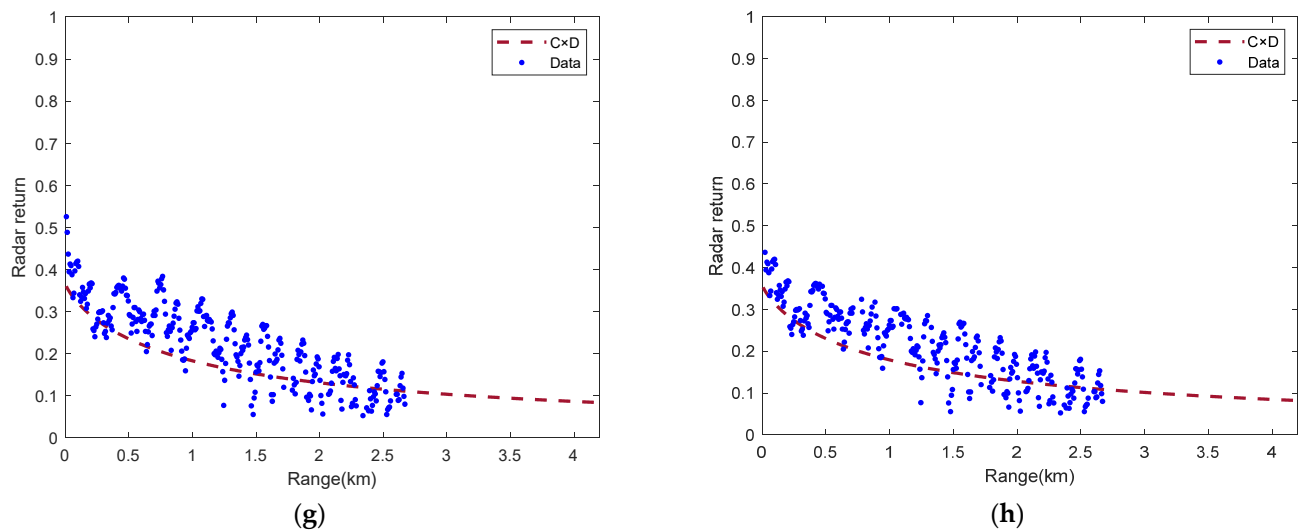


Figure 7. The estimation process for a certain azimuth attenuation horizontal component: (a) one-dimensional angle data randomly selected from Figure 2a; (b) naive estimation, where $C \times D$ is the updated attenuation function (the value of attenuation horizontal component C is 0.46); (c) first estimation (the value of attenuation horizontal component C is 0.45); (d) second estimation (the value of attenuation horizontal component C is 0.43); (e) one-dimensional angle data of about 290° which is selected in Figure 2c, where $C \times D$ is the updated attenuation function; (f) naive estimation (the value of attenuation horizontal component C is 0.63); (g) first estimation (the value of attenuation horizontal component C is 0.63); (h) second estimation (the value of attenuation horizontal component C is 0.63).

Equation (9) represents the least-squares data consistent with the radar data. Here, C_θ is the attenuation horizontal component of the azimuth θ , and a_0 , a_1 , and a_2 are parameters determined by curve fitting. The wind direction is determined by the azimuth direction corresponding to the peak point of the fitted function, i.e., the value of a_2 . Before fitting, the data in the direction of the fixture occlusion areas need to be excluded.

In calculating the wind direction, the 0° azimuth direction starts from the ship heading azimuth, so the fitted peak point is the wind direction relative to the ship heading, which is not the true wind direction. The relative wind direction is converted to the absolute wind direction. The conversion formula is as follows:

$$\theta_{wind} = \text{Rem}(\theta + \theta_{ship}, 360) \quad (10)$$

where θ_{wind} is the absolute wind direction, θ is the azimuth of the wind direction relative to the ship heading, θ_{ship} is the ship heading azimuth direction, and Rem is the operation to calculate the remainder.

3. Results

3.1. Data Overview

The radar data used here were collected using a standard X-band nautical radar and the radar configuration is shown in Table 1. The rotation period of the radar antenna is about 2.5 s, and the pulse repetition frequency is 1.3 kHz. Each radar image sequence collected here consists of 32 images, that is, each image sequence is separated by 80 s. The radar is mounted on the forward side of the ship's mainmast, approximately 25 m above sea level, next to an anemometer for measuring wind parameter information, as shown in Figure 8. The radar is connected to a wave monitoring system (HEU wave monitoring system) which digitizes and stores the radar backscattering information as a 14-bit sequence of greyscale depth images, i.e., the digitized backscattering intensity ranges from 0 to 8192. The device simultaneously collects navigation information such as heading and speed, and meteorological information such as wind direction and wind speed, when collecting the

original radar data. The reference wind data are used to verify the accuracy of the wind direction, which is measured by shipborne marine radar. It measures and records the wind direction and speed every minute.

Table 1. X-band marine radar parameters.

Radar Parameters	The Performance
Electromagnetic wave frequency	9.4 GHz
Polarization	HH
Antenna height	25 m
Antenna angular speed	24 rpm
Range resolution	7.5 m
Horizontal beam width	1.3°
Pulse width (long-pulse)	0.5 μ s
Pulse width (short-pulse)	0.06 μ s
Grazing angle	<5°



Figure 8. Radar installation position.

Figure 2a shows a radar image collected at 09:06 on 21 September 2017 with a heading of 87.9°, a wind direction of 88.99°, and a wind speed of 5.9 m/s, as indicated by the red line marking the occlusion area. It can be seen that in the approximate range of 140° to 210°, there are a number of invalid signals in the image and a fan-shaped shadow area appears. This is due to the blocking of the mainmast, which obscures the path of the electromagnetic waves, resulting in an occlusion area.

The data used for the design and validation of the wind direction retrieval algorithm based on the X-band marine radar were provided by the China Oceanic Administration (COA) during the voyage of a maritime surveillance vessel. In the experiment, anemometer and marine radar data were collected during four periods from 2 May to 25 October 2017, mainly in the sea area during the voyage from Zhejiang coast to Diaoyu Island, with a total of 3200 sets of data. Time plots of the wind data measured by the anemometer are presented in Figure 9. The data for these four different time periods are separated by vertical dashed lines and the data collection time is marked. The first period is medium-wind-speed radar data with only a mast occlusion area; the second period is high-wind-speed radar data with only a mast occlusion area; the third period is low-wind-speed radar data with only an occlusion area; and the fourth period is also high-wind-speed data, but at this time, not only is an occlusion area formed by the mast, but the radar images are also subject to interference from the stationary target; in particular, in the second half of the data, there are more fixed targets. Since the sailing ship is not specifically used to collect sea surface wind information, the data of the four time periods do not have a large range of wind directions or wind speeds. In addition, we have not collected enough radar data having enough outliers to meet the ideal conditions. However, there are also different degrees of interference.

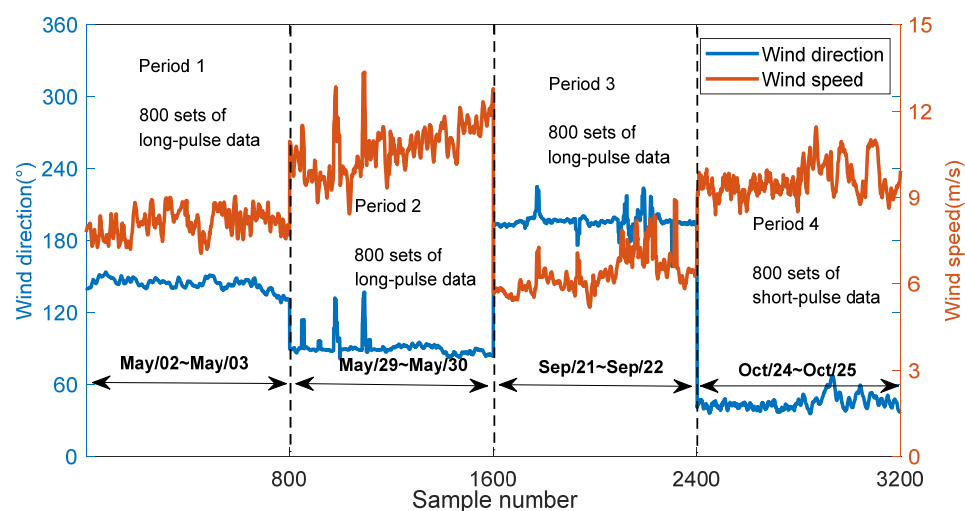


Figure 9. Wind direction (blue) and wind speed (orange) measurements acquired by an anemometer.

3.2. Wind Direction Retrieval Results

To test the proposed algorithm, the single curve-fitting method in [31] and the proposed method are applied to the above radar data. Since it must take a finite amount of time for the ocean roughness to react to wind change, unlike an anemometer, the radar may not pick up short-time-scale wind variations [32]. Therefore, 10 min averaging was applied to both the anemometer and radar wind results before computing the comparison statistics.

Before extracting the wind direction, the radar data were processed as described in Section 2.1. Figure 2 shows three different types of radar images. Figure 2a is a long-pulse radar image at low wind speed; Figure 2b is a short-pulse radar image at medium wind speed, but there are fixed targets in the radar image; and Figure 2c is a short-pulse radar image at high wind speed, but there are more fixed targets and local occlusion areas are formed by the high-intensity target in the radar image. These three types of radar images are first used to test the above two methods. Figure 10 shows the fitting results of three different kinds of radar images using the single curve-fitting method and the method based on the attenuation horizontal component. Figure 10a,c,e show the fitting results of the scatter plots for three different kinds of radar images in Figure 2a–c using the single curve-fitting method. Figure 10b,d,f show the fitting results of the scatter plots for three different kinds of radar images in Figure 2a–c using the attenuation horizontal component method. It can be seen from Figure 10a,b that the wind direction results retrieved by the two methods are both very close to the wind direction retrieved by the anemometer, and compared with the single curve-fitting method, the radar-retrieved wind direction using the method based on the attenuation horizontal component is only improved from 78° to 84° . For Figure 2a, the wind speed is only 5.9 m/s at this time. Although, the radar return in the radar image is generally low and there are more low-intensity invalid pixel dots that appear with increasing range, the single curve-fitting method can still stably retrieve the wind direction under low-wind-speed conditions. Compared with the single curve-fitting method, the attenuation horizontal component method has a certain improvement, but it is not very significant. This shows that under the condition of low wind speed, the method based on the attenuation horizontal component can improve the accuracy of wind direction retrieval to a certain extent. In addition, the data fluctuation in Figure 10b is larger than that in Figure 10a. The idea of this algorithm is based on the dependence of the wind direction on the azimuth, and the size of the data fluctuation range will affect the accuracy of the results when fitting the data. However, as long as the stable cosine wind field characteristic is found, the wind direction can be accurately retrieved. The new method obtains the attenuation horizontal component by comparing the ideal range attenuation model with the one-dimensional data in each azimuth. It can be seen from Figure 2a that the resolution of the long-pulse radar image is low, which will lead to the elimination of too many pixels

in the iterative process and cause the fluctuation in the attenuation horizontal component. However, the attenuation horizontal component can maintain a stable fluctuation range and the direction characteristic of the wind field is also clear. Therefore, it has no effect on the retrieval of wind direction. It may be observed from Figure 10c,d that, compared with single curve-fitting method, the radar-retrieved wind direction using the range attenuation method is only improved from 4° to 10° . For Figure 2b, the wind speed is as high as 9.8 m/s. Although the scanning range of the radar antenna is obscured and there is also the influence of stationary vessels on the sea surface, there are fewer fixed objects and less interference from other sources. Therefore, compared with the single curve-fitting method, the accuracy of the radar wind direction retrieved by the method based on the attenuation horizontal component is not significantly improved. The two methods have similar accuracy in the wind direction results of the above two images; this is because the interference in these two radar images is relatively limited, and the single curve-fitting method has good robustness and can stably retrieve the wind direction. Although the new method has accuracy that is similar to that of the single curve-fitting method, it has a certain improvement, which shows that our method can also accurately retrieve wind direction.

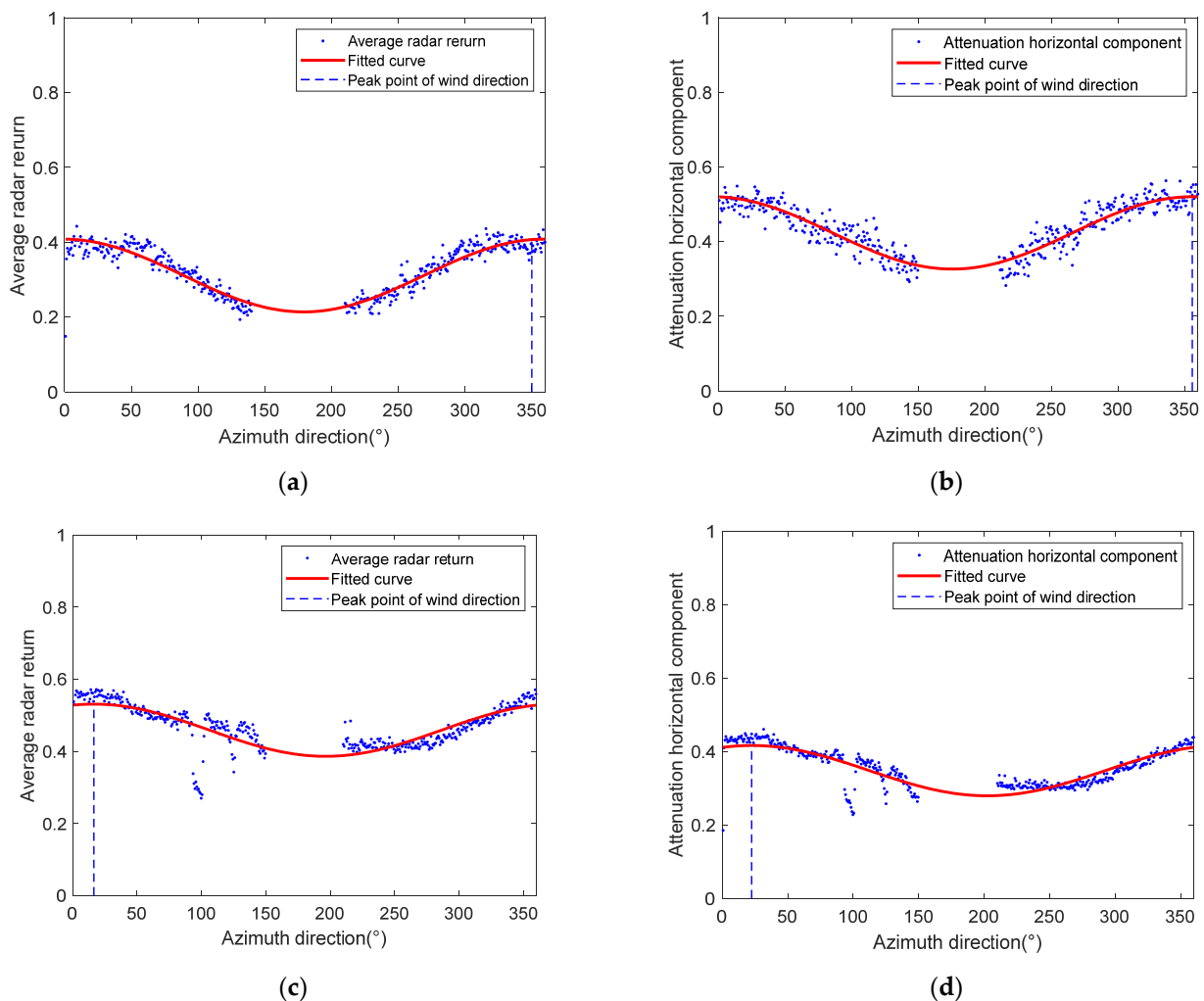


Figure 10. Cont.

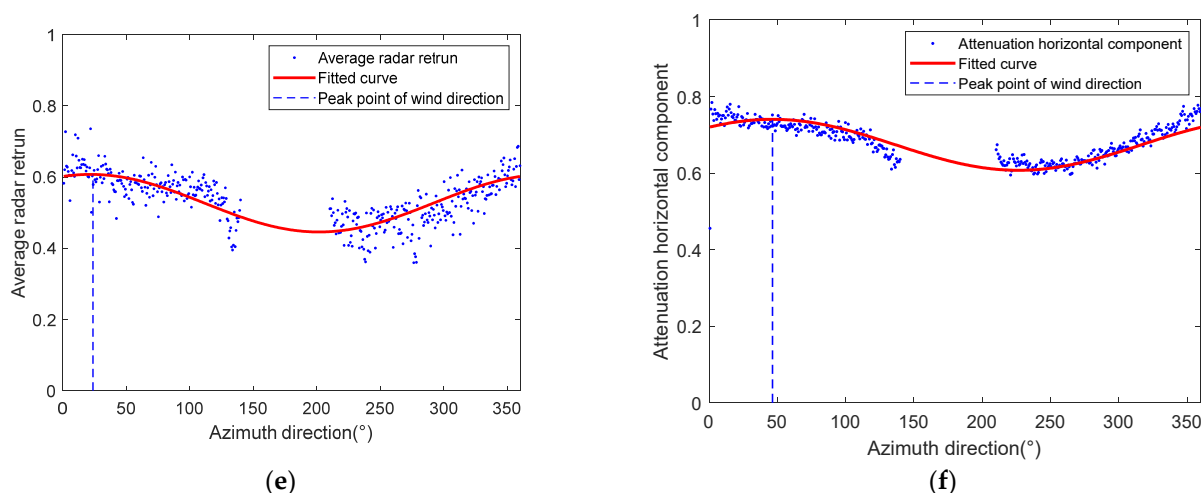


Figure 10. Curve-fitting results: (a) curve-fitting results using single curve fitting for Figure 2a (the retrieved wind direction is 78°); (b) curve-fitting results using the attenuation horizontal component method for Figure 2a (the retrieved wind direction is 84°); (c) curve-fitting results using single curve fitting for Figure 2b (the retrieved wind direction is 4°); (d) curve-fitting results using the attenuation horizontal component method for Figure 2b (the retrieved wind direction is 10°); (e) curve-fitting results using single curve fitting for Figure 2c (the retrieved wind direction is 18.5°); (f) curve-fitting results using the attenuation horizontal component method for Figure 2c (the retrieved wind direction is 47.5°).

However, it may be observed from Figure 10e,f that, compared with the single curve-fitting method, the radar-retrieved wind direction using the method based on the attenuation horizontal component for Figure 2c is improved from 18.5° to 47.5° , which is very close to the wind direction of 51° extracted by the anemometer. Combining Figures 2c and 10e shows that there are more fixed targets and interference in the radar image, and the radar electromagnetic wave will be occluded by the high target to form a local occlusion area. This will lead to a large number of deviation values in the scatter points of the single curve-fitting method, thereby reducing the accuracy of wind direction retrieval. However, the method based on the attenuation horizontal component can stably eliminate the interference caused by occlusion and targets in the iterative optimization process and accurately retrieve the wind direction, as shown in Figure 10f. In this study, different types of radar data from four time periods were tested separately. The wind data measured by the anemometer were used as a reference for comparison with the results of radar wind measurement. The wind direction results extracted from different types of data in these four time periods are shown in Figure 11. The right coordinate axis gives the reference wind speed extracted by the anemometer. The results of the four time periods for error statistics are shown in Table 2.

Table 2. Wind direction recovery error statistics: deviation and root mean square error (RMSE).

Period	Average Wind Speed	Single Curve Fitting		Attenuation Horizontal Component Method	
		Deviation ($^\circ$)	RMSE ($^\circ$)	Deviation ($^\circ$)	RMSE ($^\circ$)
1	8.1 m/s	11.4°	12.5°	8.8°	9.5°
2	10.7 m/s	11.8°	13.5°	6.0°	7.9°
3	6.3 m/s	16.8°	17.4°	5.9°	8.6°
The first half of 4	9.3 m/s	12.3°	13.1°	4.9°	7.3°
The second half of 4	9.9 m/s	24.2°	25.1°	7.9°	8.9°

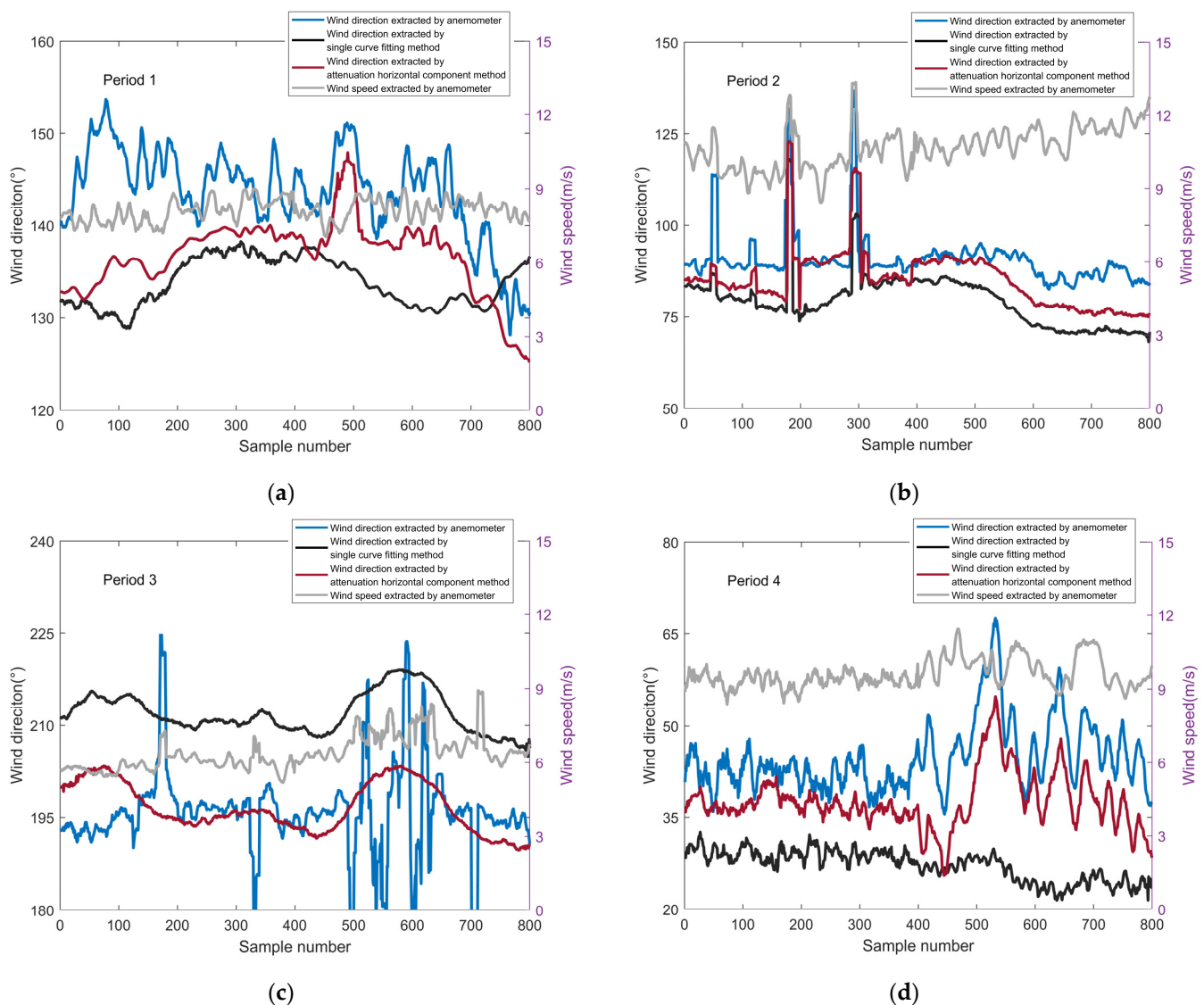


Figure 11. Comparison of the two methods with the reference wind direction: (a) “Period 1” is medium-wind-speed radar data with only a mast occlusion area; (b) “Period 2” is high-wind-speed radar data with only a mast occlusion area; (c) “Period 3” is low-wind-speed radar data with only an occlusion area; (d) “Period 4” is also high-wind-speed data but, at this time, not only is the occlusion area formed by the mast, but the radar image is also subject to interference by the stationary target; in particular, in the second half of the data there are more fixed targets.

4. Discussion

By observing Figure 11a,b, it can be seen that the wind directions retrieved by the single curve-fitting method and the method based on the attenuated horizontal component are all consistent with the anemometer data under the conditions of medium wind speed and high wind speed. Table 2 shows that, compared with the single curve-fitting method, the new method only reduces the wind direction retrieval accuracy by 2.6° in terms of deviation and 3° in terms of root mean square error for an average wind speed of 8.1 m/s, and 5.8° in terms of deviation and 5.6° in terms of root mean square error for an average wind speed of 10.7 m/s. Because the wind speed is high, the radar image data are more stable and there is less interference caused by fixed targets in the radar image. Therefore, the two methods have similar accuracy and the attenuation horizontal component method can also stably retrieve the sea surface wind direction in the case of a sea surface that is not subject to interference.

It can be observed from Figure 11c that, compared with the single curve-fitting method, the wind direction retrieved by the new method is closer to the wind direction retrieved by the anemometer. At the same time, it can be seen that there is a big difference between the attenuation horizontal component method and the anemometer at some moments. This is because the anemometer is affected by local turbulence. Even if the data are averaged within 10 min, it will still produce large errors. The radar image reflects a relatively stable sea surface state for a long time, so the wind direction result is relatively stable, which is also an advantage of radar wind measurement. The deviation and root mean square error of the wind directions obtained using the single curve-fitting method under the condition of low wind speed are 16.8° and 17.4° , respectively, and the deviation and root mean square error of the wind directions obtained using the new method are 5.9° and 8.6° , respectively. The new method only reduces the wind direction retrieval accuracy by 10.9° in terms of deviation and 8.8° in terms of root mean square error for an average wind speed of 6.3 m/s. Under the condition of low wind speed, the radar return in the radar image is generally low and there are more low-intensity invalid pixel dots that appear with increasing range. It can be seen from Table 2 that, although the wind direction retrieval accuracy of the single curve-fitting method is reduced under low-wind-speed conditions, it also has certain robustness. Compared with the single curve-fitting method, the attenuation horizontal component method has a certain improvement, but it is not very significant. This shows that under the condition of low wind speed, the method based on the attenuation horizontal component can improve the accuracy of wind direction retrieval to a certain extent.

For the first half of the fourth period, the deviation and root mean square error of the wind directions obtained using the single curve-fitting method are 12.9° and 13.1° , respectively, and the deviation and root mean square error of the wind directions obtained using the new method are only 4.9° and 5.5° , respectively. The new method reduces the wind direction retrieval accuracy by 8° in terms of deviation and 7.6° in terms of root mean square error. It can be observed from Figure 11d that, in the first half of the data, the new method has a certain improvement compared with the single curve-fitting method. This is because the fixed targets and outliers of the first half of the data are relatively limited, and the improvement in the attenuation horizontal component method is also relatively limited. However, the deviation and root mean square error of the wind directions obtained using the single curve-fitting method are 24.2° and 25.1° , respectively, whereas the deviation and root mean square error of the wind directions obtained using the new method are only 7.9° and 8.9° , respectively. The new method reduces the wind direction retrieval accuracy by 16.3° in terms of deviation and 16.2° in terms of root mean square error. In the second half of the data, the wind direction result of the single curve-fitting method compared to the anemometer has a large error, and the attenuation horizontal component method can stably retrieve the wind direction. Due to the interference of more targets and outliers in the second half of the data, not only will high-intensity outliers be generated, but local occlusion areas will also be generated behind targets, as shown in Figure 2c. In the initial estimation of the attenuation horizontal component, the interference is initially eliminated by setting the weight of the invalid low-intensity pixels to zero. In the subsequent iterative estimation process, a threshold is added to further eliminate other noises and outliers. The method based on the attenuation horizontal component can remove unstable pixels caused by occlusion and targets in the iterative optimization process and improve the accuracy of wind direction retrieval.

In most cases, compared with the single curve-fitting method, the wind direction results retrieved by the attenuated horizontal component method are not significantly improved and have similar accuracy. The new method can improve the accuracy of wind direction retrieval to a certain extent in the case of low wind speed. In the case of more interference, the wind direction accuracy can be significantly improved. It is important to note that the results of this paper are only based on the analysis of data that were not affected by rainfall pollution.

5. Conclusions

This paper presents a new technique for extracting wind direction from X-band marine images. The method is based on the attenuation horizontal component of radar images. The interference caused by fixed targets and outliers can be processed to further improve the results by analyzing the one-dimensional data of radar images. An ideal range attenuation model for the radar image is derived from the selected ideal attenuation data. Then, the ideal attenuation model is compared with the one-dimensional data for each azimuth to find the attenuation horizontal component. The unstable values in the one-dimensional data are further processed by iterative optimization. The wind direction is obtained by building a cosine function of the attenuation horizontal component and the azimuth direction.

The new method was applied to a total of 3200 X-band radar images collected over four time periods. The radar-derived wind directions were compared with those measured by anemometers. The comparison results show that, for medium and high wind speeds, the new method maintains an accuracy close to that of the single curve-fitting method in [31]. Under the condition of low wind speed, the deviation and root mean square error of wind direction were only increased by 10.9° and 8.8° , respectively. In the case of obscured areas and target interference, the new method improves the retrieved wind direction deviation and root mean square error by 16.3° and 16.2° , respectively. In summary, the method based on the attenuation horizontal component can improve the wind direction retrieval accuracy in the case of more fixed targets.

Due to the limitations of the data, we have not collected a significant quantity of sea state data that meet the ideal conditions, and the interference of the collected radar data is also quite limited. Furthermore, the wind direction retrieved by method in [31] is also quite reliable and stable. However, compared with the traditional single curve-fitting method, our method still has a certain improvement, because it does not need to make a preliminary judgment on the outliers and can stably filter out the interference in the process of retrieving the wind direction. Of course, we regret that, because of the problem of the data, the best experimental results are not presented. This is also the direction we need to take to further the research in the future. In addition, the range attenuation method also has some limitations. Because two iterations of optimization are required in the calculation of the attenuation horizontal component, the whole process takes more time compared to the single curve-fitting method. In addition, the accuracy of the algorithm is also limited by the ideal attenuation model, and a better model can minimize the error of the algorithm. In the future, the algorithm needs to be further studied. It is necessary to find a more suitable ideal attenuation model and develop a method based on range attenuation to improve the wind speed inversion accuracy of radar images.

Author Contributions: Conceptualization, Z.L. and H.Y.; methodology, H.Y.; software, H.Y.; validation, H.Y., H.W. and Z.L.; formal analysis, H.Y., H.W. and Z.L.; investigation, H.Y.; resources, Z.L.; data curation, H.Y.; writing—original draft preparation, H.Y.; writing—review and editing, H.Y.; visualization, H.Y.; supervision, Z.L. and H.W.; project administration, H.Y., H.W. and Z.L.; funding acquisition, Z.L. All authors have read and agreed to the published version of the manuscript.

Funding: This research received no external funding.

Data Availability Statement: The raw/processed data required to reproduce these findings cannot be shared at this time as the data are also part of an ongoing study.

Acknowledgments: The authors would like to thank the anonymous peer reviewers for their valuable comments. The authors also sincerely appreciate the associate editor's enthusiastic help and responsible support.

Conflicts of Interest: The authors declare no conflict of interest.

References

1. Thornhill, E.; Wall, A.; McTavish, S.; Lee, R. Ship anemometer bias management. *Ocean Eng.* **2020**, *21*, 107843. [[CrossRef](#)]
2. Zhang, Y.; Liu, F.; Lu, Z.; Wei, Y.; Wang, H. Multi-anemometer optimal layout and weighted fusion method for estimation of ship surface steady-state wind parameters. *Ocean Eng.* **2022**, *266*, 112793. [[CrossRef](#)]
3. Wang, H.; Qiu, H.; Lu, Z.; Wang, L.; Akhtar, R.; Wei, Y. An Energy Spectrum Algorithm for Wind Direction Retrieval From X-Band Marine Radar Image Sequences. *IEEE J. Sel. Top. Appl. Earth Obs. Remote Sens.* **2021**, *14*, 4074–4088. [[CrossRef](#)]
4. Al-Habashneh, A.A.; Moloney, C.; Gill, E.W.; Huang, W. The effect of radar ocean surface sampling on wave spectrum estimation using x-band marine radar. *IEEE Access* **2018**, *6*, 17570–17585.
5. Senet, C.M.; Seemann, J.; Flampouris, S.; Ziemer, F. Determination of bathymetric and current maps by the method disc based on the analysis of nautical x-band radar image sequences of the sea surface. *IEEE Trans. Geosci. Remote Sens.* **2007**, *46*, 2267–2279. [[CrossRef](#)]
6. Shen, C.; Huang, W.; Gill, E.W.; Carrasco, R.; Horstmann, J. An algorithm for surface current retrieval from x-band marine radar images. *Remote Sens.* **2015**, *7*, 7753–7767. [[CrossRef](#)]
7. Lund, B.; Graber, H.C.; Campana, J.; Terrill, E. Near-surface current shear measured by marine X-band radar. In Proceedings of the 2015 IEEE/OES Eleventh Current, Waves and Turbulence Measurement (CWTM), St. Petersburg, FL, USA, 2–6 March 2015.
8. Lund, B.; Graber, H.C.; Hessner, K.; Williams, N.J. On shipboard marine X-band radar near-surface current “calibration”. *J. Atmos. Ocean. Technol.* **2015**, *32*, 1928–1944. [[CrossRef](#)]
9. Hessner, K.G.; El Naggar, S.; von Appen, W.-J.; Strass, V.H. On the Reliability of Surface Current Measurements by X-Band Marine Radar. *Remote Sens.* **2019**, *11*, 1030. [[CrossRef](#)]
10. Ludeno, G.; Postacchini, M.; Natale, A.; Brocchini, M.; Lugni, C.; Soldovieri, F.; Serafino, F. Normalized scalar product approach for nearshore bathymetric estimation from x-band radar images: An assessment based on simulated and measured data. *IEEE J. Ocean. Eng.* **2018**, *43*, 221–237.
11. Flampouris, S.; Ziemer, F.; Seemann, J. Accuracy of bathymetric assessment by locally analyzing radar ocean wave imagery. *IEEE Trans. Geosci. Remote Sens.* **2008**, *46*, 2906–2913. [[CrossRef](#)]
12. Bell, P.S. Shallow water bathymetry derived from an analysis of x-band marine radar images of waves. *Coast. Eng.* **1999**, *37*, 513–527.
13. Honegger, D.A.; Haller, M.C.; Holman, R.A. High-resolution bathymetry estimates via X-band marine radar: 1. beaches. *Coast. Eng.* **2019**, *149*, 39–48.
14. Honegger, D.A.; Haller, M.C.; Holman, R.A. High-resolution bathymetry estimates via X-band marine radar: 2. Effects of currents at tidal inlets. *Coast. Eng.* **2020**, *156*, 103626.
15. Atkinson, J.; Esteves, L.; Williams, J.; Bell, P.; McCann, D. Nearshore Monitoring With X-Band Radar: Maximizing Utility in Dynamic and Complex Environments. *J. Geophys. Res. Ocean.* **2021**, *126*, e2020JC016841.
16. Lund, B.; Haus, B.K.; Graber, H.C.; Horstmann, J.; Carrasco, R.; Novelli, G.; Guigand, C.M.; Mehta, S.; Laxague, N.J.M.; Özgökmen, T.M. Marine X-Band Radar Currents and Bathymetry: An Argument for a Wave Number-Dependent Retrieval Method. *J. Geophys. Res. Ocean.* **2020**, *125*, e2019JC015618.
17. Chen, Z.; He, Y.; Zhang, B. An automatic algorithm to retrieve wave height from x-band marine radar image sequence. *IEEE Trans. Geosci. Remote Sens.* **2017**, *55*, 5084–5092.
18. Nieto-Borge, J.C.; Hessner, K.; Jarabo-Amores, P.; De, L.M.D. Signal-to-noise ratio analysis to estimate ocean wave heights from x-band marine radar image time series. *IET Radar Sonar Navig.* **2008**, *2*, 35–41.
19. Liu, X.; Huang, W.; Gill, E.W. Wave height estimation from ship-borne x-band nautical radar images. *J. Sens.* **2016**, *2016*, 7. [[CrossRef](#)]
20. Liu, X.; Huang, W.; Gill, E.W. Estimation of significant wave height from x-band marine radar images based on ensemble empirical mode decomposition. *IEEE Geosci. Remote Sens. Lett.* **2017**, *14*, 1740–1744.
21. An, J.; Huang, W.; Gill, E.W. A self-adaptive wavelet-based algorithm for wave measurement using nautical radar. *IEEE Trans. Geosci. Remote Sens.* **2015**, *53*, 567–577.
22. Navarro, W.; Velez, J.C.; Orfila, A.; Lonin, S. A shadowing mitigation approach for sea state parameters estimation using X-band remotely sensing radar data in coastal areas. *IEEE Trans. Geosci. Remote Sens.* **2019**, *57*, 6292–6310.
23. Streßer, M.; Horstmann, J.; Baschek, B. Surface Wave and Roller Dissipation Observed With Shore-Based Doppler Marine Radar. *J. Geophys. Res. Ocean.* **2022**, *127*, e2022JC018437. [[CrossRef](#)]
24. Wu, L.C.; Doong, D.J.; Lai, J.W. Influences of nononshore winds on significant wave height estimations using coastal X-band radar images. *IEEE Trans. Geosci. Remote Sens.* **2021**, *60*, 4202111. [[CrossRef](#)]
25. Wright, J. Backscattering from capillary waves with application to sea clutter. *IEEE Trans. Antennas Propag.* **1966**, *14*, 749–754.
26. Huang, W.; Liu, X.; Gill, E.W. Ocean wind and wave measurements using x-band marine radar: A comprehensive review. *Remote Sens.* **2017**, *9*, 1261.
27. Lee, P.H.Y.; Barter, J.D.; Caponi, E.; Caponi, M.; Hindman, C.L.; Lake, B.M.; Rungaldier, H. Wind-speed dependence of small-grazing-angle microwave backscatter from sea surfaces. *IEEE Trans. Antennas Propag.* **1996**, *44*, 333–340.
28. Trizna, D.B.; Carlson, D.J. Studies of dual polarized low grazing angle radar sea scatter in nearshore regions. *IEEE Trans. Geosci. Remote Sens.* **1996**, *34*, 747–757. [[CrossRef](#)]

29. Vicen-Bueno, R.; Horstmann, J.; Terril, E.; de Paolo, T.; Dannenberg, J. Real-time ocean wind vector retrieval from marine radar image sequences acquired at grazing angle. *J. Atmos. Ocean. Technol.* **2013**, *30*, 127–139.
30. Chen, Z.; He, Y.; Zhang, B.; Qiu, Z. Determination of nearshore sea surface wind vector from marine X-band radar images. *Ocean Eng.* **2015**, *96*, 79–85. [[CrossRef](#)]
31. Lund, B.; Graber, H.C.; Romeiser, R. Wind retrieval from shipborne nautical x-band radar data. *IEEE Trans. Geosci. Remote Sens.* **2012**, *50*, 3800–3811.
32. Liu, Y.; Huang, W.; Gill, E.W.; Peters, D.K.; Vicen-Bueno, R. Comparison of algorithms for wind parameters extraction from shipborne x-band marine radar images. *IEEE J. Sel. Top. Appl. Earth Obs. Remote Sens.* **2015**, *8*, 896–906. [[CrossRef](#)]
33. Yu, H.; Wang, H.; Lu, Z. Wind-Direction Estimation from Single X-Band Marine Radar Image Improvement by Utilizing the DWT and Azimuth-Scale Expansion Method. *Entropy* **2022**, *24*, 747. [[CrossRef](#)] [[PubMed](#)]
34. Wei, Y.; Liu, Y.; Song, H.; Lu, Z. A Method of Rainfall Detection from X-band Marine Radar Image Based on the Principal Component Feature Extracted. *IEEE Geosci. Remote Sens. Lett.* **2023**, *20*, 3501105.
35. Kim, M.-S.; Kwon, B.H. Rainfall Detection and Rainfall Rate Estimation Using Microwave Attenuation. *Atmosphere* **2018**, *9*, 287. [[CrossRef](#)]
36. Christofilakis, V.; Tatsis, G.; Chronopoulos, S.K.; Sakkas, A.; Skrivanos, A.G.; Peppas, K.P.; Nistazakis, H.E.; Baldoumas, G.; Kostarakis, P. Earth-to-Earth Microwave Rain Attenuation Measurements: A Survey On the Recent Literature. *Symmetry* **2020**, *12*, 1440.
37. Wang, Y.; Huang, W. An algorithm for wind direction retrieval from X-band marine radar images. *IEEE Geosci. Remote Sens. Lett.* **2016**, *13*, 252–256. [[CrossRef](#)]
38. Liu, X.; Huang, W.; Gill, E.W. Wind direction estimation from rain-contaminated marine radar data using the ensemble empirical mode decomposition method. *IEEE Trans. Geosci. Remote Sens.* **2017**, *55*, 1833–1841.
39. Huang, W.; Liu, Y.; Gill, E.W. Texture-analysis-incorporated wind parameters extraction from rain-contaminated X-band nautical radar images. *Remote Sens.* **2017**, *9*, 166. [[CrossRef](#)]
40. Chen, X.; Huang, W.; Haller, M.C. A novel scheme for extracting sea surface wind information from rain-contaminated x-band marine radar images. *IEEE J. Sel. Top. Appl. Earth Obs. Remote Sens.* **2021**, *14*, 5220–5234.
41. Dankert, H.; Horstmann, J.; Rosenthal, W. Ocean surface winds retrieved from marine radar-image sequences. In Proceedings of the IEEE International Geoscience and Remote Sensing Symposium, Anchorage, AK, USA, 20–24 September 2004.
42. Dankert, H.; Horstmann, J.; Rosenthal, W. Ocean wind fields retrieved from radar-image sequences. *J. Geophys. Res. Oceans.* **2003**, *108*, 3353–3362. [[CrossRef](#)]
43. Dankert, H.; Horstmann, J.; Rosenthal, W. Wind-and wave-field measurements using marine X-band radar-image sequences. *IEEE J. Ocean. Eng.* **2005**, *30*, 534–542. [[CrossRef](#)]
44. Dankert, H.; Horstmann, J. A marine radar wind sensor. *J. Atmos. Ocean. Technol.* **2007**, *24*, 1629–1642. [[CrossRef](#)]
45. Zheng, Y.; Lin, S.; Kang, S.B.; Xiao, R.; Gee, J.C.; Kambhamettu, C. Single-image vignetting correction from gradient distribution symmetries. *IEEE Trans. Pattern Anal. Mach. Intell.* **2012**, *35*, 1480–1494. [[CrossRef](#)]
46. Cho, H.; Lee, H.; Lee, S. Radial bright channel prior for single image vignetting correction. *Eur. Conf. Comput. Vis.* **2014**, 8690, 189–202.

Disclaimer/Publisher’s Note: The statements, opinions and data contained in all publications are solely those of the individual author(s) and contributor(s) and not of MDPI and/or the editor(s). MDPI and/or the editor(s) disclaim responsibility for any injury to people or property resulting from any ideas, methods, instructions or products referred to in the content.